PCCP

Accepted Manuscript

ROYAL SOCIETY OF CHEMISTRY

www.rsc.org/pccp

Journal Name

RSCPublishing

ARTICLE

Following ORR Intermediates Adsorbed on a Pt Cathode Catalyst during Break-in of a PEM Fuel Cell by *in operando* X-ray Absorption Spectroscopy.

D.E. Ramaker[a], A. Korovina[a], V. Croze[b], J. Melke[b], and C. Roth[b,c]

Cite this: DOI: 10.1039/xoxxoooooox

Received ooth January 2012,
Accepted ooth January 2012

DOI: 10.1039/xoxxoooooox

www.rsc.org/

In operando X-ray Absorption Spectroscopy data using the Δμ X-ray Absorption Near Edge Spectroscopy (XANES) analysis procedure is used to follow the ORR intermediate adsorbate coverage on a working catalyst in a PEMFC during initial activation and break-in. The adsorbate coverage and log i (Tafel) curves reveal a strong correlation, i.e., an increase in adsorbate intermediate coverage poisons Pt sites thereby decreasing the current. A decrease in Pt-O bond strength commensurate with decrease in potential causes a sequence of different dominant adsorbate volcano curves to exist, namely first O, then OH, and then OOH exactly as predicted by the different ORR kinetics mechanisms. During break-in, the incipient O coverage coming from exposure to air during storage and MEA preparation is rather quickly removed, compared to the slower and more subtle nanoparticle morphological changes, such as the rounding of the Pt nanoparticle edges/corners and smoothing of the planar surfaces, driven by the nanoparticle's tendency to lower its surface energy. These morphological changes increase the Pt-Pt average coordination number, decrease the average Pt-O bond strength, and thereby decrease the coverage of ORR intermediates, allowing increase in the current.

Introduction

1. The nature of catalyst changes during fuel cell break-in

A catalyst enhances the rate of a reaction (lowers its activation energy) by participating in a reaction or changing its path; but it is not consumed or presumably changed by it. This is the definition given for a catalyst in many basic textbooks[1]. However, in practice the catalyst often changes slowly or deteriorates over its operational lifetime, and most often it must be activated or undergo a break-in period before it becomes fully functional. Figure 1 schematically illustrates the activity of a typical Pt based (pure Pt or PtM bimetallic) oxygen reduction reaction (ORR) catalyst as used in a PEM (proton exchange membrane) fuel cell. In Figure 1, the abscissa indicates the number of current-voltage (I-V) cycles carried out (0.6 – 1.0 V at 16 sec/cycle using USDOE protocol[2] or similar I-V procedure using square or triangular waves[3,4,5]). Targets have been set by USDOE indicating that less than 40% of the beginning of life (BOL) activity should be lost after 30000 cycles, if it is to satisfy durability limits[2]. These 30k cycles are usually applied as an accelerated stress test (AST) to mimic the stress a catalyst might undergo in a PEMFC equipped automobile due to the large number of stops and starts expected during a normal auto lifetime. These start/stops are very detrimental to the catalyst due to the voltage spikes that can occur at these times, apparently more so than during the normal operation of the fuel cell, when the voltage is held relatively constant.[2,3,5]

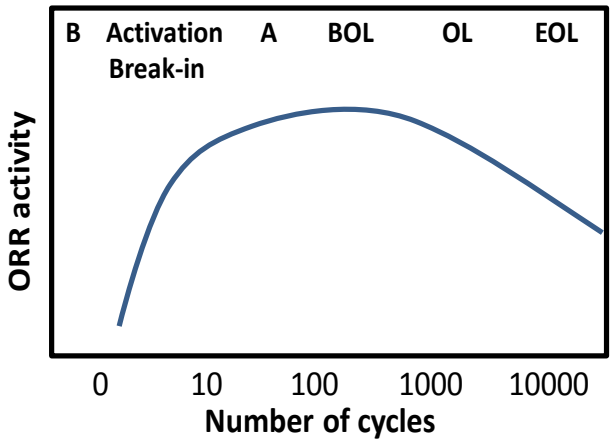

Figure 1 Schematic showing relative ORR mass activity as function of number of current-voltage cycles and the life stages: B(before break-in), activation, A (after break-in), BOL (beginning of life), OL (operational lifetime), and EOL (end of life).

The durability of a catalyst is as critical to its ultimate utility in practice as its beginning of life (BOL) activity. This is why it has been studied now for many years. These studies have revealed that it is the repeated oxidation and reduction of the catalysts that can cause particle growth (Ostwald ripening), Pt

dissolution, M metal leaching in the case of a Pt-M catalyst and other changes occurring in particle morphology. However, the higher the BOL activity, the more the decline can be tolerated, even though a correlation is generally found between the BOL activity and decline rate; i.e., the higher the BOL activity, the faster the catalyst deteriorates[6]. All of this suggests that the activation process during break-in might also be critical to the ultimate functionality of the catalyst. Despite this, very few critical studies using in–situ spectroscopic characterization tools have been reported to study the changes in a catalyst during the activation process.

In this work we use x-ray absorption spectroscopy (XAS) to study the early stage activation or break-in of a carbon-supported Pt/VC catalyst in a working fuel cell. A Pt/VC catalyst prepared in an MEA (membrane electrode assembly) is examined via *in operando* XAS using the Δμ XANES analysis method[7,8] to follow not only the initial reduction of the catalyst but also the adsorbed ORR intermediates existing during early operation of an as-prepared catalyst. In addition a catalyst is studied after an extended period (7 days) in an operating fuel cell; i.e., in both cases without initial I-V cycling so that the first MEA is not broke-in, and the second can be assumed to be fully activated.

Following the ORR intermediate species, such as O, OH, OOH, and coverage on catalyst surfaces is critical for understanding the fundamental kinetic mechanisms in a fuel cell. The Δμ XANES isolation technique has proven to provide adsorbate identity and binding site information on both the anode or cathode under *in situ*[7,9] and *in operando* conditions[8,10,11,12] and even in high temperature PBI-phosphate based fuel cells[13]; therefore, it was used in this work to better understand the types of adsorbate species present during initial break-in on the cathode side. Here we distinguish between *in situ* (in an electrochemical environment involving an electrolyte) vs. *in operando* (in an operating fuel cell with anode and cathode and a current flowing). With both time dependent[11] and spatial resolution[10] we have previously published *in operando* data showing the effects of current (proton) flow and inhomogeneity's in fuel and air flow.

In this work, adsorbed species were identified and their coverage was followed as a function of current (or potential) in an operating fuel cell. Moreover, since data were collected as a function of current, Tafel plots allowed for the observation of kinetic trends with changing adsorbate species on the catalyst surface. These results show a direct correlation between the adsorbed ORR intermediates and the Tafel curves, and point to the nature of the subtle changes that the Pt catalysts undergo during the activation process.

2. ORR Kinetics

The ORR kinetics has been well modeled with the rate expression[14,15]:

$$i = nF\, k\, c_{O2} \exp(-\alpha FV/RT)\ \exp(-\gamma \Delta G_{rds}/RT)\ (1-\theta_{tad}), \quad (1)$$

where RT/αF is the Tafel slope, and the factors out front are the number, n, of electrons transferred (one) in the rate determining step (RDS), the oxygen concentration, c_{O2}, and the exchange rate constant, k, of the rds. Here, V is the overpotential, and the important parameters for this discussion are θ_{tad} and ΔG_{rds}. θ_{tad} is the total adsorbate (tad) coverage of all intermediates and other anions and ΔG_{rds} is the activation energy of the rds. The possible intermediates on the surface can be any or all of the following: O, O_2, OH, OOH, H_2O_2, and H_2O and nearly all of these have been somehow associated with the rds in previous reports far too numerous to review here.

We have previously[12] differentiated the reactions as the rds vs. primary adsorbate determining step, or 'pads'. Clearly the rds involves getting the initial adsorbate on the surface in either of two mechanisms:

Dissociative: $O_2 + (H^+ + e^-) + 2* \rightarrow OH* + O*$ (2)

Non-dissociative: $O_2 + (H^+ + e^-) + * \rightarrow OOH*$ (3)

The fact that eq. 1 models the kinetics, with the proper dependence on c_{O2}, pH, n, and V (Tafel slope), points to the reactants on the left side of 2) or 3) being involved in the rds. Further the constant activation energy (ΔG_{rds} = 40 kJ/mol) determined from Arrhenius plots for Pt and Pt-M catalysts[16], points to the rds involving some weakly bonded intermediate, perhaps physisorbed O_2 or even O_2 in the inner Helmholtz layer. This is because a more tightly bonded adsorbate on the surface, such as OH* or OOH* would change ΔG_{rds} with Pt-O bond strength (i.e. changed Pt surface), assuming a linear Bronsted, Evans, Polanyi (BEP) relation between the activation energy and intermediate binding energy[17].

The primary adsorbate making up the θ_{tad} will be determined by the slowest reaction on the surface (i.e. the pads not the rds). This has been proposed as one of the reactions[18,19,20]:

Diss: $OH* + (H^+ + e^-) \rightarrow H_2O + *$ (4)

Non-Diss, OOH*: $OOH* + * \rightarrow O + OH*$ (5)

Non-Diss, HOOH: $HOOH* + * \rightarrow 2OH*$; (6)

leading to the dissociative, peroxyl, or hydrogen peroxide mechanisms respectively. Here the * indicates an empty Pt site, and the ad* indicates an adsorbate on a Pt site. In the dissociative mechanism[19,20], as the name implies, the Pt-O_2 bond is so strong that the bonding involves electron transfer from Pt to the O_2 and therefore simultaneous breaking of the O_2 bond as in (2). The OOH* and HOOH* mechanisms imply a weaker non-dissociative Pt-O_2 bond, and therefore 1 or 2 (H^++e-) additions are needed to help break the O_2 bond. Thus the nature of the slow step on the surface, the pads, is very much determined by the nature of the Pt catalysts (particle size, shape and microstructure), because the pads is determined by the strength of the Pt-O bond involving the ORR intermediates adsorbed on the surface. Therefore the pads primarily determines the ORR rate through the $\theta_{tad.}$

Wang et al.[21] have carefully considered Tafel slope changes, adsorbate species and the ORR on Pt(111) with their double trap kinetic model, assuming the dissociative model above. The following kinetic equations were derived from that model for the 4-e- ORR in acidic media in a fuel cell:

$½\ O_2 + * \rightarrow O*$ Dissociative Adsorption(DA) (7)

$½\ O_2 + (H^+ + e^-) + * \rightarrow OH*$ Reductive Adsorption (RA) (8)

$O* + (H^+ + e^-) \rightarrow OH*$ Reductive Transition (RT) (9)

$OH^* + (H^+ + e^-) \rightarrow H_2O + *$ Reductive Desorption (RD) (10)

These reactions can be summarized further as:

$\frac{1}{2} O_2 \rightarrow OH^*$ (via RA or via DA+RT) $\rightarrow H_2O$ (via RD). (11)

Wang et al.[21] showed that the RA mechanism is fastest below 0.7 V (vs. RHE) while the DA is above, thus O* dominates as adsorbed intermediate above 0.7 and OH* below. We will see that our data agree with this conclusion.

Experiment and Data Analysis

1. Samples preparation and spectroscopy

Two MEA's were considered in this work, both had the same composition for the cathode (20 wt% Pt on VC from Etek) and anode (20 wt.% Pt-Ru 1:1 on Vulcan carbon). The catalyst coated membranes (CCMs) were prepared by spraying an ink on the polymer electrolyte Nafion®115 membrane. The ink was fabricated by dispersion of the catalyst powder in high purity water and 5% Nafion® solution using an ultrasonic tip. The ink was air-brushed onto the membrane in several layers successively, after each previous layer had been left to dry (vacuum table heated to 130 °C at the end of the last step). The metal loading of the electrode with size of 5x5 cm^2 was determined to be 1.7 mg cm^{-2} by gravimetric analysis.

X-ray absorption spectroscopy measurements were carried out at beamline X1 at Hasylab, Hamburg in fluorescence mode during electrochemical operation using a test bench by MAGNUM and an *in operando* fuel cell with X-ray transparent Kapton foil windows. The CCM was sandwiched between Au-coated stainless steel endplates with integrated, interdigitated flow fields. A small part of the anode catalyst layer (less than 10x2 mm^2) was removed to avoid collecting data on the Pt anode. Between flow field and electrode a Toray TGP H 90 gas diffusion layer was placed. Hydrogen was supplied at 150 ml/min in H_2/O_2 operation, oxygen (4.5 grade) was supplied at 75 ml/min by flow controllers (Bronkhorst). The cell was operated with anode humidification at 80°C and 75°C cell temperature.

The first MEA was an 'as prepared' catalyst without break-in or operational conditioning and hence will be labeled "0d" to contrast it with the second identical MEA which was placed in an operating fuel cell for seven days in the lab and then transported to Hamburg for XAS analysis, hence labeled "7d". The spectra were collected with each succeeding data point collected at lower current (increasing V) except for 0d1 which were measured with increasing current (decreasing V). This direction for 0d1 was chosen to better follow the reduction of the initial oxide with decreasing potential and time on this as prepared catalysts. The first pass was collected in 'normal' fluorescence mode, with scans taking about 20-35 minutes immediately followed by the second set of scans in the "quick" fluorescence mode, with scans only taking about 3 minutes. The results suggest no difference between the normal and quick method of collection, other than decreased noise levels in the normal XAS data mode. The numerous data points collected allow for a very detailed analysis of the cathode processes.

2. XANES, Δμ extraction and EXAFS analysis

Raw XAS data were analyzed using the Δμ analysis technique[7,8] and the ATHENA code in the IFEFFIT suite of programs[22]. After background subtraction, a normalization procedure was conducted over a short range of ~30 – 60 eV, relative to the Pt L_3 edge (11564eV) to avoid some small glitches just below and above this range; subsequently, energy calibration is further applied to the raw data to account for and remove slight shifts in the data arising from photon beam drift or energy uncertainties arising from the monochromator.[7] To isolate the effect of surface adsorbates at different potentials, the Δμ signature was extracted by subtracting a spectrum taken at a potential that is low or adsorbate free, $\mu(V_{ref})$. In previous work[7] this $\mu(V_{ref})$ was generally taken in the double layer region around 0.5 V; however, in these *in operando* fuel cell measurements, the cleanest surface is generally found at high current in the diffusion limited region, when the diffusion of O_2 limits the amount of adsorbates on the surface. The Δμ at potential V are then obtained using $\Delta\mu = \mu(V) - \mu(V_{ref})$. A similar procedure is applied to theoretical data obtained with the help of full multiple scattering ab-initio calculations using the FEFF8 code[23]. Theoretical Δμ signatures are essential for the determination of adsorbates at specific potentials and overall interpretation of results.

EXAFS fitting was done with Artemis[22] using a single Pt-Pt path in the region $2 < k^3 < 10$ $Å^{-1}$ and $1.8 < R < 3.8$ Å.

3. FEFF Calculations

Theoretical Δμ signatures from the FEFF8 code[23] are necessary because they allow for qualitative identification of the experimental adsorbates and binding sites. As previously discussed by Teliska et al.[7], a Janin-type Pt_6 cluster[24] was utilized due to its functional structure. Similar to experiment, the theoretical Δμ is isolated by: $\Delta\mu_{Theory} = \mu(Ads/Pt_6) - \mu(Pt_6)$. A μ is generated for a clean Pt_6 Janin cluster and another μ is generated after an adsorbate (Ads) is placed on that Pt_6 Janin cluster at different binding sites and at different bond lengths. In general, Teliska et al.[7] modeled adsorbed oxygen at a bond distance of 2.0Å. An O bound in an atop site represents an OH, while that in an n-fold site represents an O adsorbate consistent with an O atom's preference for two-fold bonding. The present *in operando* PEMFC results required further calculations beyond the typical mono-oxygen containing species, O(H), namely di-oxygen species, such as OOH. Peroxyl was modeled by an OOH species in an atop site on the Pt surface with orientation as shown in Fig. 3.

In our previous work a Pt_6 cluster has been used most often to model the experimental Pt clusters[7-13], as this highly asymmetrical cluster provides for all of the possible common binding sites (fcc, hcp, bridged, and atop) and is asymmetrical so that it does not introduce any "surface resonances", which might arise from a more symmetric cluster[25], and yet the

cluster is sufficiently large to account for the change in Pt-Pt scattering and new Pt-Ad scattering introduced by the adsorbate. Recently, calculations with increasingly bigger clusters (Pt_6, Pt_{13} and Pt_{25}) were compared and found to give similar Δμ signatures[26], and DFT calculations on slabs were shown to also give similar signatures as FEFF8 for O/Pt and CO/Pt[27]. These calculations and others[28] show that the dominant contributions to Δμ are "local" to the Pt-O bond, and hence small clusters already give qualitative agreement with experiment[29,30], certainly sufficient to identify the binding site. Since the experimental data is an average over a wide array of particles sizes and shapes in a catalyst, any further attempt to improve on the model cluster to find more quantitative agreement between the experimental and theoretical signatures is deemed to be fruitless.

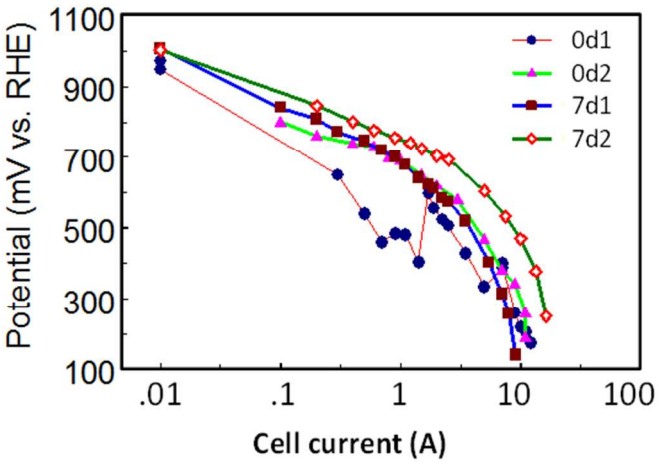

Figure 2 Tafel plots (potential vs log I without corrections for IR and O_2 diffusion limit) for the four indicated data sets (1st or 2nd run (1 or 2) on as-prepared 0d and after 7 days operating in a fuel cell (7d).

RESULTS and DISCUSSION

1. Tafel Plots

The performance of the catalysts can be evaluated through Tafel analysis of the I-V curves obtained during the XAS measurement, Fig. 2. The Tafel plots for the 4 different data sets clearly show an improvement in performance of the catalyst during the 2nd cycle. 0d1 is initially heavily oxidized, since it was run as prepared with initial potential at 920 mV. 0d2 already shows significant improvement, probably because during the latter part of the 0d1 run, the catalyst was held for periods of ~20 minutes per point at low reducing potentials, during which most of the surface oxygen has been removed. The 7d1 Tafel plot shows a slight reduction in performance compared to 0d2. As mentioned above, the fuel cell was run for about a week then stopped and transported to the beamline for measurements, thus it is not difficult to imagine some oxidation or water hydration during transportation and setup of the cell causing some degradation. Analysis of the XAS data below will clearly reveal the subtle differences in the catalysts properties during these 4 runs.

It should be noted that these Tafel plots reflect simply the log of the current (log i); i.e. no iR or diffusion limit (DL) corrections have been applied. The current vs potential curve typically has regions where the kinetics losses dominate, but as the current increases the iR losses become large, and eventually as the O_2 DL is reached at very high current (low potential), an additional drop in current arises. To account for these additional voltage losses, it is common practice to measure the cell resistance and subtract off the iR loss, and further to plot $\log[(i-i_{lim})/i_{lim}]$ rather than just log i to extend the linear region to higher current.[25] After these corrections, the slope generally reflects primarily kinetic losses, so that a Tafel slope (eq. 1) of $RT/\alpha F$ = 120 mV/decade is obtained, where α is the transfer coefficient generally accepted to be ½.[31] At potentials above 0.85 V and at very low current, the Tafel slope often falls even lower, to 60 mV/decade; this is attributed to reduction of the O(H) (O or OH) residing on the surface with this O(H) arising from water activation[32]. Only one point in each curve in Fig. 1 exists above 0.85 V, so the very low Tafel slope arising from water activation cannot be seen. The slopes below 0.85 found in Fig. 2 with values between 150-250 mV/decade are much above the pure kinetic value of 120 mV/decade, showing that the iR and DL losses are significant. However in figures below, we are primarily interested in highlighting **changes** in Tafel slope as the adsorbate coverages change, thus we prefer to plot just log i in this work, without including the iR and DL corrections which might confound or even hide these slope changes.

2. Δμ XANES signatures

Fig. 3 shows the typical experimental Δμ signatures extracted from the 0d1 set compared to theory. The theoretical Δμ signatures are given for 3 different adsorbates, O, OH, and OOH. The O Δμ signature shown in Fig. 3, and reported many times previously as the characteristic O/Pt signature[7], is compared with that for OH/Pt. The Pt-O bond length is a bit longer for OH than for O, and the additional H causes more backscattering (blue shaded area), so the total OH/Pt signature is given by the solid blue line. The O/Pt signature is shifted up by about 2eV from the OH signature and has a larger negative contribution around 10-20 eV, consistent with that found by Teliska and coworkers[7]. Comparison with the experimental curves suggests the dominant adsorbate species at potentials between 401 to 801 eV is OH/Pt. The Pt-O bond length is still longer for the peroxyl radical, and now the OH outside the first O atom introduces the shaded area in red[12] This feature is clearly visible in the 261 and 204 mV spectra although somewhat narrower than in the theoretical spectrum. Thus the Δμ lineshape suggests that the dominant adsorbate at low currents is O, then OH dominates at intermediate potentials, and finally OOH dominates at the highest currents as found previously[12]. Data for the 0d2, 7d1 and 7d2 sets show similar changes in lineshapes.

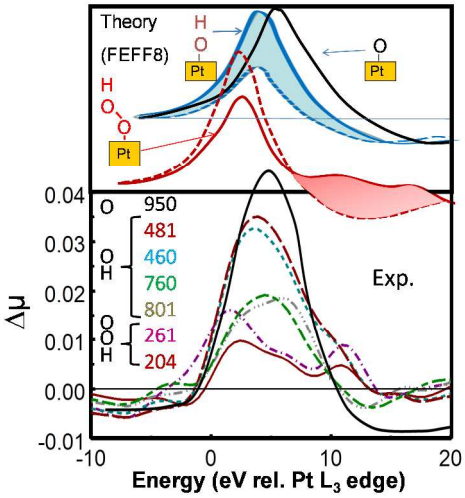

Figure 3 Δμ = μ(V) - μ(250 mV) for catalyst 0d1 at the indicated cell potentials (mV). Also indicated are FEFF8 results for the indicated adsorbates with orientation as shown (dashed lines show Δμ for just the O atom at the appropriate Pt-O bond length, solid for the full adsorbate such as OH* in blue and OOH* in red). The contribution from the second O in the OOH* is highlighted in red, that from the H in the OH* in blue, as determined from the difference in Δμ with and without the second atom. The H "outside" the second O in OOH* is not included in the FEFF8 calculations as it contributes little to the Δμ signal.

3. Correlation of |Δμ| with Tafel curves

Figures 4 and 5 show plots of the Tafel curves for the 0d1 and 0d2 runs respectively, along with the magnitude of the Δμ maxima (|Δμ|) between 3-5 eV (relative to the Pt L_3 edge as shown in Fig. 3). This magnitude |Δμ| reflects the relative coverage of adsorbates on the Pt surface. |Δμ| may not be exactly proportional to the total adsorbate coverage, but the |Δμ| (magnitude not shape) as extracted here in the 3-5 eV region will be reasonably similar for O, OH, and OOH (as shown by the FEFF8 calculations) because all 3 involve a single Pt-O bond. Further, the conclusions reached in this paper do NOT depend on a rigid proportionality of |Δμ| with coverage, rather the change in Δμ signature (shape) with current (or potential) is more critical. The labels on top of Figs. 4 and 5 indicate the dominant component of the adsorbate coverage as indicated from the Δμ signatures in Fig. 3 for the 0d1 and Od2 runs. We choose not to attempt any further isolation of the separate O*, OH*, and OOH* components here (such as might be done with a linear combination fitting procedure to the experimental curve with theoretical standards), because the behavior of |Δμ| for example in Fig. 5 suggests rather clearly that the regions where each component dominates do not strongly overlap.

The dominant component, shifting from O to OH to OOH with increasing current (decreasing potential), is exactly as expected based on the ORR kinetics as summarized above. At high potential the Pt-O bond is strong so O_2 dissociation proceeds the fastest, as indicated by the DA mechanism, eq. 7. As the Pt-O bond strength decreases and the activation energy for H^+ addition decreases to higher current (lower potential), the RA reaction, eq. 8 becomes fastest, increasing the amount of OH. At still higher current and lower potential, the Pt-O bond becomes so weak that O_2 bond scission becomes difficult so OOH appears on the surface; i.e. the non-dissociative mechanism, eq. 5, becomes the pads. The production of HOOH at low potentials is well known from rotating disc electrode (RDE) experiments[33] as the adsorbed OOH* adds another H^+ and produces a ring current.

The measured Tafel curves in Figs. 4 and 5 correlate nicely with the Δμ XANES measured relative adsorbate coverages on the surface. To highlight this correlation, we have drawn the straight dashed line in Figs. 4 and 5 through the points with slope of about 200 mV/dec; this slope reflecting not only the ORR kinetics but iR and O_2 diffusion losses as noted above. This dashed line represents the so called "ideal" Tafel curve when the coverage of ORR intermediates is low; indeed it is determined in Fig. 5 in the region where the coverage of OH* is low and then extended to both higher and lower currents. This same line is then drawn in Fig. 4. In Fig. 5, when the experimental Tafel curve falls below this line, the adsorbate coverage is high, poisoning Pt sites and slowing the total ORR rate; i.e., the experimental Tafel curve falls below the "ideal" when the O* coverage is high at low current, and when the OOH* coverage is high at high current. This is the more normal situation also seen for both of the 7dn scans, not shown. The experimental Tafel curve for the 0d1 scan in Fig. 4 falls below the "ideal" most when the OH* coverage is large, but also appears to deviate significantly again when the O* coverage increases to very low current.

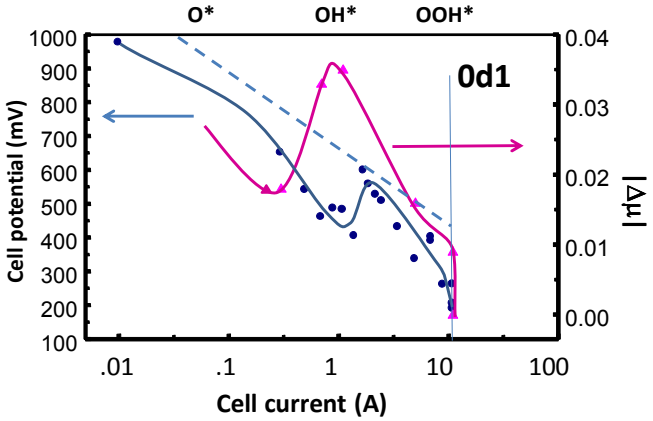

Figure 4 Plot of Δμ magnitude around 5 eV (pink triangles) as shown in Fig. 3 and the Tafel plot (log i) (blue circles) vs cell current for the 0d1 run. The dashed blue line serves as the "ideal" current as discussed in the text, and the vertical line indicates the current limit caused by the O_2 diffusion limit. .

The sharp drop below the "ideal" at high currents in both cases clearly arises from the O_2 diffusion limit; however, as noted, the increase in OOH* coverage and ultimate production of only the 2 e- reduction to H_2O_2 causes the current to drop below ideal levels prior to the diffusion limit.

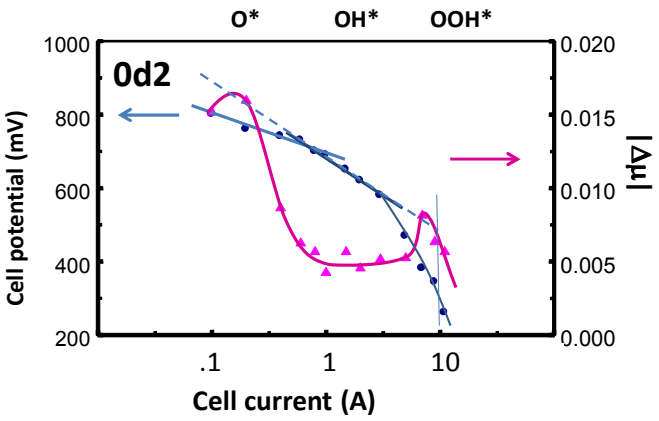

Figure 5 Same as Figure 4 but now for the 0d2 run. Δμ magnitude (adsorbate coverage respectively) shown by pink triangles, blue circles mark the cell potential with cell current

4. Nature of catalyst changes during break-in

A more complete understanding of the subtle changes in the catalysts occurring during the break-in period can now be obtained by comparing, as in Fig. 6, the coverage of ORR intermediates for the 1st and 2nd runs on the two different MEA's. Note the factor of ½ on the 0d1 plot, highlighting the larger amount of O(H)* intermediates on the initial as-prepared 0d catalysts. To more easily understand these changes in ORR intermediate coverage, we show a schematic in Fig. 7 of the adsorbate coverage expected when the Pt-O bond strength is relatively "strong", compared to when it is "weak". Both cases show the three regions where first O*, then OH*, and finally OOH* dominates due to decreasing Pt-O bond strength, but the relative magnitudes of these volcano-like peaks are different. With increasing current (decreasing potential), the O* coverage is expected to decrease faster on the weak surface and the OH* volcano will begin later and stay smaller, but the OOH* volcano will get bigger before the O_2 diffusion limit sets in. Comparison of the experimental adsorbate coverage with the schematic curves, clearly points to a decrease in average Pt-O bond strength on run 2 vs 1, with the corresponding 7d MEA showing less O(H)* than the 0d, so that the Pt-O bond strength decrease occurs in the order 0d1 > 7d1 > 0d2 > 7d2.

What can account for this trend? Clearly the as-prepared 0d catalyst is initially heavily oxidized as it was exposed to air during preparation, but this oxide is quickly (5-20 min) "reacted" off relative to the 200 minutes time scale on which the XAS data were acquired. Thus the changes seen in Fig. 6 reflect more a change in Pt-O bond strength, on the Pt surface. We conclude that the very nature of the Pt sites is changing, namely the Pt-Pt coordination must be increasing, as simple bond-order conservation dictates that with increasing Pt-Pt coordination, the Pt-O bond strength decreases. This is why small Pt particles bond O stronger than large particles[7,27] but the differences here do not necessarily reflect particle size, but rather surface roughness or particle shape. With break-in, the very small particles may be growing, but most of the particles are simply losing their sharp edges and corners, and are becoming more round or at least cubo-octahedral in shape, and some of the faces may become less rough and more ordered; these rough surfaces left after the oxide removal. All of these changes will increase the Pt-Pt coordination, and surely decrease the average Pt-O bond strength.

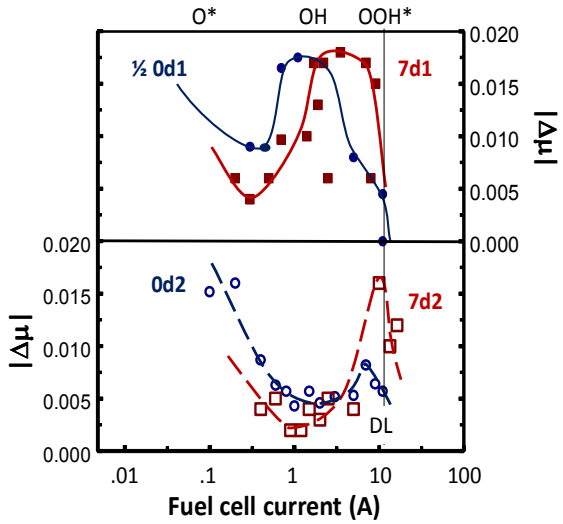

Figure 6 Comparison of the |Δμ| magnitude for the 4 different data passes (1st and 2nd on the two MEAs) as indicated. The vertical line indicates the O_2 diffusion limit where the adsorbate coverage goes very small because the O_2 reduction rate exceeds the diffusion rate of O_2 to the surface.

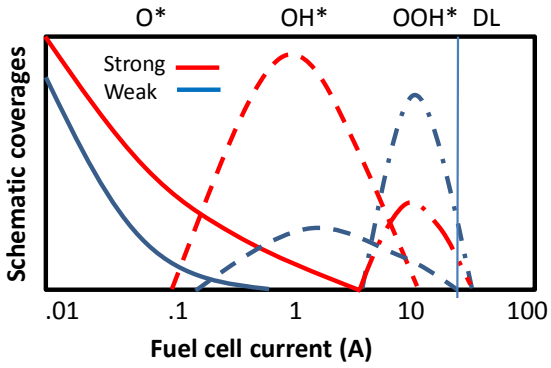

Figure 7 Schematic showing the expected relative O*, OH*, and OOH* adsorbate volcano's for the strong and weak Pt-O bond strength.

These subtle morphology changes in the Pt nanoparticles are rather difficult to follow with EXAFS or even with other structural techniques. Nevertheless, Fig. 8 shows EXAFS data for the indicted catalysts along with Pt foil, and the estimated fit parameters using a single Pt-Pt path. EXAFS data are shown only for the catalysts at the highest currents possible, i.e., near the diffusion limit when most of the adsorbates are absent from the surface. This ensures that the EXAFS is reflecting the nearly clean metallic Pt clusters, rather than the reduction in N that occurs when the catalyst is partially

oxidized or even when substantial adsorbates are present[7]. The relatively small Pt-O feature around 1.6 Å in Fig. 8 for all catalysts confirms the absence of significant oxygen containing adsorbates at these high currents, consistent with that shown by the Δμ magnitudes. Note the usual reduction in Pt-Pt distance (R) for the small clusters compared to Pt foil, and the larger Debye-Waller (σ^2) factor.[28] The σ^2 for the catalysts was fixed to the average obtained for the 4 clusters so as to highlight the change in N_{Pt-Pt}, as the usual large correlation between N and σ^2 otherwise obscures these changes.[22] N_{Pt-Pt} was fixed at 12 for the Pt foil giving a reasonable experimental estimate for the many-body S_o^2 factor of 0.873 and fixed for all other fits.[28] The N's around 9 for the catalysts are consistent with the nanoparticle size of 2-3 nm.[28] As expected, N_{Pt-Pt} does slightly increase with break-in reflecting the tendency for the nanoparticles to decrease their surface area by rounding the corners and smoothing the rough faces left after the oxide removal. The Δμ data reflect the resultant reduction in the Pt-O bond strength.

It should be noted that both the Pt-Pt CN and ORR activity increases slightly after 1 cycle during the break-in period. This is certainly different than during the aging process (i.e. after 10k or 30k cycles in Fig. 1) when a Pt-Pt CN increase means a reduction in electrochemical surface area (ECSA) assuming smooth spherical nanoparticles, and this drop in ECSA is easily confirmed by CV H_{upd} studies[6,34]. The subtle changes during break-in cannot be so easily confirmed with H_{upd} studies, because of variable full H coverage on such rough surfaces[35,36] and other difficulties with porous/rough electrodes[37]. These differences highlight the different particle morphology changes occurring. During break-in the particles are becoming more round with decreasing surface roughness and therefore increasing both the specific and mass ORR activity. During aging the particles are increasing in size, and the mass activity decreases because of a loss in surface area. Both particle changes result from the nanoparticle's thermodynamic drive to reduce its surface area during cycling, but the decreasing surface roughness occurs kinetically much faster than particle growth.

Although certainly high resolution TEM (such as HAADF) techniques[34,38] are able to follow the morphological changes indicated here, they must be carried out *in situ*. In situ TEM[39] or more specifically sometimes called environmental or liquid cell TEM (ETEM or LCTEM) has been used to study metal nanoparticle catalysts under both gas phase and electrochemical conditions, when nanoparticle nucleation, growth, and even particle morphology changes have been seen[39-42] but we are not aware of any TEM observations of such changes during real Pt/C cathode break-in. By following the strong changes in ORR intermediate coverage of O, OH, and OOH, *in operando* with XAS, we can "infer" and therefore follow these subtle changes in the Pt nanoparticle.

5 Conclusions

In operando XAS data using the Δμ XANES analysis procedure enables one to follow the ORR intermediate adsorbate coverage on a working catalyst in a PEMFC. These studies reveal the following:

Catalyst	N_{Pt-Pt} ± 10%	R(Å) ± 0.1	E_o (eV) ± 2	σ^2 fixed
Pt foil	12.0	2.75	6.00	.006
0d1	8.12	2.72	2.97	.008
0d2	8.90	2.72	3.01	.008
7d1	8.89	2.71	3.05	.008
7d2	8.92	2.72	3.48	.008

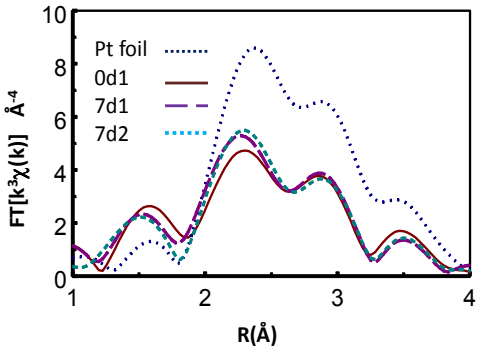

Figure 8 FT EXAFS data of the indicated catalysts along with Pt foil, and the estimated parameters from a single Pt-Pt path fit.

- The adsorbate coverage and log i (Tafel) curves reveal a strong correlation, i.e., an increase in adsorbate intermediate coverage poisons Pt sites thereby decreasing the current; thus highlighting the importance of the $(1-\theta_{tad})$ factor in the rate equation, eq. 1
- A decrease in Pt-O bond strength resulting from a decrease in potential (increasing current) causes a sequence of different dominant adsorbate volcano curves to exist, namely first O, then OH, and then OOH exactly as predicted by the different ORR kinetics mechanisms.
- During break-in, the oxide coverage resulting from exposure to air during preparation, is rather quickly removed (5-20 min), compared to the more subtle morphological changes (over 100's min), such as the rounding of the Pt nanoparticle edges and corners and smoothing of the rough planar surfaces left after the oxide removal.
- The morphological changes during break-in increase the Pt-Pt average coordination number and thereby decrease the average Pt-O bond strength, decrease the relative heights of the intermediate adsorbate volcano curves and increase the current due to a reduced fraction of poisoned Pt sites.

Acknowledgements

Thanks are due to E. Welter, M. Herrmann and K. Klementiev at the XAS beamline X1, Hasylab, Hamburg (Germany), and L. Giebeler and M. Mazurek for their help during the XAS collection. Financial support for AK from the Achievements Rewards for College Scientists (ARCS) Foundation and the

George Washington University and for CR from the Deutsche Forschungsgemeinschaft is gratefully acknowledged.

Notes and references

[a] Chemistry Dept., George Washington University, Washington, DC 20052

[b] Institute for Materials Science, Technische Universität Darmstadt, Darmstadt, Germany

c Current address: Angewandte Physikalische Chemie, Freie Universität Berlin, D-14195 Berlin

1 P.W. Atkins, **PHYSICAL CHEMISTRY**, W.H. Freeman and Co, 3rd ed. 1986, p724.

2 US Council for Automotive Research, LLC, US Drive Fuel Cell Tech Team, accessed January 6, 2014, , http://www.uscar.org/guest/teams/17/U-S-DRIVE-Fuel-Cell-Tech-Team

3 A. Marcu, G. Toth, S. Kundu, L.C. Colmenares and R.J. Behm, J. Power. Sources 2012, 215, 266-273.

4. F. Ettingshausen, J. Kleemann, A. Marcu, G. Toth, H. Fuess, C. Roth, *Fuel Cells,* 2011,**11**,238-245

5 A. Marcu, G. Toth, R. Behm, R. J.,2013, *Electrochemical Test Procedures for Accelerated Evaluation of Fuel Cell Cathode Catalyst Degradation. Fuel Cells*. doi: 10.1002/fuce.201300138

6 A. Kongkanand, 2013 Annual Merit Review, US Department of Energy Hydrogen and Fuel Cells Program, accessed January 6, 2014,http://www.hydrogen.energy.gov/pdfs/review13/fc087_kongkanand_2013_o.pdf

7 M. Teliska, W.E. O'Grady, D.E. Ramaker, *J. Phys. Chem. B,* 2004, **108**, 2333; *B* 2005, **109**, 8076; M. Teliska, V.S. Murthi, S. Mukerjee, D.E. Ramaker, *J. Electrochem. Soc.,* 2005**, 152A**, 2159 – 2169.

8 C. Roth, N. Benker, T. Buhrmester, M. Mazurek, M. Loster, H. Fuess, D.C. Koningsberger, D.E. Ramaker, *J. Am. Chem. Soc*. 2005, **127** 14607- 14615; F.J. Scott, C. Roth, D.E. Ramaker, *J. Phys. Chem. C*, 2007, **111**, 11403-11413; F.J. Scott, S. Mukerjee, D.E. Ramaker, *J. Electrochem. Soc.* 2007, **154**, A396-A406; *J. Phys. Chem. C* 2010, **114**, 442–453.

9 A. Kongkanand, J.M. Ziegelbauer, *J. Phys. Chem. C*, 2013, **116**, 3684-3693.

10 D. Dixon, A. Habereder, M. Farmand, S. Kaserer, C. Roth, D. E. Ramaker, *J. Phys. Chem. C*, 2012, **116,** 7587–7595.

11 J. Melke, A. Schoekel, D. Dixon, C. Cremers, D.E. Ramaker, and C. Roth, *J. Phys. Chem. C*, 2010, **114**, 5914; J. Melke, A. Schökel, F. Ettinghausen, D. Dixon, C. Cremers, D. E. Ramaker, C. Roth, *J. Phys. Chem. C*, 2012, **116,** 2838–2849.

12 D.E. Ramaker, K. Caldwell, Q. Jia, Q, J. Zeigelbauer, S. Mukerjee, *J. Am. Chem. Soc.* submitted 2014; K. Caldwell, D.E. Ramaker, Q. Jia, S. Mukerjee, J. Ziegelbauer, *J. Phys. Chem. C*, submitted 2014

13 S. Kaserer, K.M. Caldwell, D.E. Ramaker, C. Roth, *J. Phys. Chem. C* 2013, **117**, 6210-6217; also to be published.

14 M.R. Tarasevich, A. Sadlowski, E. Yeager, in **COMPREHENSIVE TREATISE IN ELECTROCHEMISTRY**; J.O. Bockris, B.E. Conway, E. Yeager, S.U.M. Khan, R.E. White, Eds.; Plenum, New York, 1983; 301-398; F. Uribe, M.S. Wilson, T. Springer, S. Gottesfeld, in **PROCEEDING OF THE WORKSHOP IN STRUCTURAL EFFECTS IN ELECTROCATALYSIS AND OXYGEN ELECTROCHEMISTRY** 92-11; D. Scherson, D. Tryk, M. Daroux, X. Xing, Eds., The Electrochem. Soc.: Pennington, NJ, 1992; 494-509.

15 V.R. Stamenkovic, B.S. Mun, M. Arenz, K.J.J. Mayrhofer, C.A. Lucas, G. Wang, P.N. Ross, N.M. Markovic, *Nat. Mat*. 2007, **6**, 241-247.

16 M. Watanabe, M. Wakisaka, H. Yano, H. Uchida, *ECS Trans*. 2008, **16**, 199-206; Proc. EICCS, Sapporo, Jn, Mar. 14-19, 2009.

17 T. Bligaard, J.K. Norskov, S. Dahl, J. Matthiesen, C.H. Christensen, J. Shested, *J. Catal*. 2004, 224, 206-217.

18 J.A. Keith, T. Jacob, *Angew. Chem. Int. Ed.,* 2010, **49**, 9521-9525.

19 J.A. Herron, J. Jiao. K. Hahn, G. Peng, R.R. Adzic, M. Mavrikakis, *J. Electrocatal*. 2012, **3**, 192-202; A.U. Nilekar, M. Mavrikakis, *Surf. Sci.* 2008, **602**, L89-L94; J.L. Zhang, M.B. Vukmirovic, M. Xu, M. Mavrikakis, R.R. Adzic, *Ang. Chem. Int. Ed*. 2005, **44**, 2132.

20 J. Rossmeisl, G.S. Karlberg, T. Jaramillo, J.K. Norskov, *Faraday Disc*. 2008, **140**, 337-346.

21 J.X.Wang, J. Zhang, R.R. Adzic, *J. Phys. Chem. A,* 2007, **111**, 12702-12710; J.X. Wang, F.A. Uribe, T.E. Springer, J. Zhang, R.R. Adzic, *Faraday Discuss*, 2008, **140**, 347-362.

22 B. Ravel, M. J. Newville. J. *Synch. Rad.* 2005, **12**, 537

23 A.L. Ankudinov, B. Ravel, J.J. Rehr, S.D. Conradson, *Phys. Rev. B* 1998, **58**, 7565-7576.

24 E. Janin, H. von Schenck, M. Göthelid, U.O. Karlsson, M. Svensson, *Phys. Rev. B*, 2000, **61**, 13144-13149

25 D.E. Ramaker and D.C. Koningsberger, Phys. Rev. Lett. 89, 2002, **139**, 701.

26 Q. Jia, J.M. Ziegelbauer, Z. Liu, Z. Yu, M. Trahan, K. Caldwell, D.E. Ramaker, S. Mukerjee, "In Situ Investigation of the Structural and Electronic Properties of Well-defined Dealloyed Pt_1Co_1/C Nanoparticles", submitted.

27 Y. Lei, J. Jelic, L.C. Nitsche, R. Meyer, J. Miller, Top. Catal. 2011, **54**, 334-338; N. Guo, B.R. Fingland, W.D. Williams, V.F. Kispersky, J. Jelic, W.N. Delgass, F.H. Ribeiro, R.J. Meyer, J.T. Miller, Phys. Chem. Chem. Phys. 2010, **12**, 5678-5693.

28 D.E. Ramaker, D.C. Koningsberger, Phys. Chem. Chem. Phys. **2010**, 12, 5514.

29 C. Roth and D.E. Ramaker, **MODERN ASPECTS OF ELECTROCHEMISTRY**, ed. by C.G. Vayanes, Springer, New York, **2010**, 159-201.

30 C. Roth and D.E. Ramaker, **FUEL CELL SCIENCE: THEORY, FUNDAMENTALS, AND BIOCATALYSIS**, Edited by Andrzej Wieckowski and Jens K. Nørskov, **2010**, John Wiley & Sons, 511-535.

31 S.Gottesfeld, in **FUEL CELL CATALYSIS**, M. Koper ed, John Wiley &Sons, Inc. 2009, Chapter 1, 1-30.

32 J.X. Wang, N.M. Markovic, R.R. Adzic, *J. Phys. Chem. B* 2004, **108**, 4127.

33 H.A. Gasteiger, S.S. Kocha, B. Sompalli, F.T. Wagner, *Appl. Catal. B,* 2005, **56**, 9-35; W. Vielstich, A. Lamm, H.A. Gasteiger, **HANDBOOK OF FUEL CELLS: FUNDAMENTALS, TECHNOLOGY, AND APPLICATIONS**; Wiley, Hoboken, NJ, 2003

34 C.E. Carlton, B. Han, A. Kongkanand R.S. Kukreja, L. Gan, R. O'Malley, Y. Shao-Horn, P. Strasser, F.T. Wagner, in preparation.

35 B.J. Kip, F.B.M. Duivenvoorden, D.C. Koningsberger, and R. Prins, J. Catal. 1987, **105**, 26-38.

36. Y. Ji, A.M.J. van der Eerden, V. Koot, P.J. Kooyman, J.D. Meeldijk, B.M. Weckhuysen, D.C. Koningsberger, J. Catal. 2005, **234,** 376-384.
37. R.W. Lindström, K. Kortsdottir, M. Wesselmark, A. Oyarce, C. Lagergren, G. Lindbergh, J. Electrochem. Soc. 2010 **157**: B1795-B1801; ECS Trans. 2009, **25**, 1211-1220
38 Z. Liu, H. Xin, Z. Yu, Y. Zhu, J. Zhang, J.A. Mundy, D.A. Muller, F.T. Wagner, *J. Electrochem. Soc.* 2012, **159**, F1-F6.
39 T.W. Hansen, J.B. Wagner, P.L. Hansen, S. Dahl, H. Topsoe, C.J.H. Jacobsen, *Science*, 2001, 294, 1508-1510.
40 S. Takeda, H. Yoshida, *Microscopy,* 2013, 62, 193-203.
41 S.B. Simonsen, I. Chorkendorff, S. Dahl, M. Skoglundh, J. Schested, S. J. Helveg, *J. Am Chem. Soc.,* 2010,**132**, 7968-7975.
42 H. Yoshida, Y. Kuwauchi, J.R. Jinschek, K. Sun, S. Tanaka, M.Kohyama, S. Shimada, M. Haruta, S. Takeda, *Science*, 2012, 335, 317.